Imperial College London

École Polytechnique Fédérale de Lausanne

Department of Physics

MSci Physics with a Year in Europe

Description of Coherent Beam Instabilities in the Presence of Space Charge Forces using the Circulant Matrix Model

CID: 01329810

Laboratory for Particle Accelerator Physics

Supervisors: Dr. X. Buffat (CERN) and Dr. T. Pieloni (EPFL)

Word Count: 10,037

September 16, 2020

Preface

This work was undertaken at CERN in Meyrin, Switzerland as part of the Laboratory for Particle Accelerator Physics group (LPAP) based at EPFL, during my exchange year from Imperial College London. The work in this report is based on the code written to simulate beam beam interactions called 'BimBim' which was developed by my supervisor Xavier Buffat for his PhD thesis in 2015. We added the effect of space charge forces for an airbag distribution and Gaussian distribution. The investigative work on the effect of space charge in the presence of wake fields has been done with the help and guidance of my supervisor.

The effect of COVID-19 has been minimal on my project in that the aims have remained the same, but it meant I was no longer able to work with my supervisor at CERN in person, but instead had to communicate via Skype from home.

Abstract

Low energy hadron synchrotrons face significant limitations in the number of particles per bunch because of the direct electromagnetic interaction of beam particles, known as space charge. This report aimed to improve previous models showing how space charge affects the limitations of transverse mode coupling instabilities due to electromagnetic wake fields by using a Gaussian charge distribution in the code BimBim which implements the circulant matrix model. The space charge tune shift modes were compared for the airbag in a linear potential and Gaussian distributions. We used the airbag in a square-well distribution as a benchmark. The main result was the comparison of the transverse mode coupling instabilities (TMCI) generated due to space charge and wake fields for the airbag and Gaussian distributions. We confirmed with theory that sufficiently strong space charge can suppress the instabilities caused by wake fields alone. For the airbag distribution, positive mode coupling was found to be a result of our approximation to a finite ring width. The Gaussian distribution showed that when considering multiple radial modes, increasing space charge induced new types of instabilities that cannot be attributed to numerical artefacts. We thus find that space charge suppresses the negative TMCI due to wake fields and causes positive mode coupling.

Contents

Chapter 1

Introduction

The study of beam dynamics is essential in accelerator physics. Particle accelerators are powerful tools which can answer fundamental questions about the universe. The knowledge acquired from accelerator experiments can be applied to a wide range of fields such as medicine for radiation cancer therapies, solid state physics and material science research [1]. We are constantly looking at ways to improve the capabilities of accelerators such as increasing the number of particles per bunch, also known as the bunch intensity, and energy at which it is possible to accelerate particles. However, there are many limitations in our ability to confine these highly intense and energetic beams with current technology. The collective effect we are focusing on is called space charge, which is the the direct electromagnetic interaction between particles in the beam, changing the dynamics of the beam [2]. Low energy hadron synchrotrons are limited in the number of particles per bunch due to the effect of space charge [3]. We will be investigating how space charge affects the limitation due to coherent beam instabilities caused by the interaction with self-induced electromagnetic wake fields in space charge dominated machines. Wake fields generate instabilities as a result of the interaction of the charged beam with its surroundings [2].

This project aimed to accurately model the effect due to space charge and wake fields on beam stability in low energy hadron synchrotrons by extending a code that simulates the beam self-induced wake fields called BimBim to include space charge forces. First we implemented the action of space charge in BimBim by calculating the space charge kick of one cell on another for a given beam discretisation in longitudinal phase space and chose the appropriate parameters for computation in the one turn matrix. We then looked at the simulated space charge tune shifts produced by an infinitely thin ring of charge called the airbag, in a linear potential and Gaussian beam charge distributions. A benchmark to this work is the airbag in a square-well potential [4]. We then explored a wide range of parameters to reproduce unstable conditions with wake fields and added the effect of space charge, focusing on the transverse mode coupling instability threshold for the airbag and Gaussian distributions.

1.1 Motivation

If we review previous work, we see that the modelling of space charge in beam dynamics is not novel, with the first work done by M. Blaskiewicz in 1998 using an airbag distribution in a square-well potential [4]. We have approached the modelling of space charge with a different computing framework than previously attempted, notably we use a Gaussian distribution to represent a more realistic spread of beam charge. The motivation for this different approach is that when using the simplified distribution of the airbag model, space charge seems to suppress the instability due to the wake fields, which is not observed in practice for some machines, for example in the Super Proton Synchrotron at CERN [3]. Previous work that used a Gaussian distribution was only applicable for high space charge and thus was not realistic for modelling the dynamics in an accelerator [5]. Our approach is unique in that it can be used for any strength of space charge, covering also the range of low space charge where observations show different behaviour to that previously predicted.

Chapter 2

Accelerator Physics

We can start by looking at characteristic properties of particle accelerators. This work is appropriate for a synchrotron, which is a circular particle accelerator that keeps the radius of the circulating particles approximately constant by synchronising the revolution frequency with the energy increase per turn [6]. It is comprised, in essence, of radio frequency (RF) cavities to accelerate the particles, dipole magnets to bend the particle trajectory and higher order magnets such as quadrupoles to focus and defocus the beam and sextupoles to correct for chromatic aberrations. Synchrotrons accelerate particles to higher energies such that we describe them by their relative velocity with respect to the speed of light $\beta_r = v/c$ and their relativistic mass factor γ_r given by [6]

$$\gamma_r = \frac{1}{\sqrt{1-\beta_r^2}}. \tag{2.1}$$

The Frenet-Serret coordinate system is used to describe particle motion in a synchrotron, as shown in Fig. 2.1, where s is the distance along the accelerator, periodic over the circumference of the ring, $C = 2\pi R$. The relativistic momentum of the particle, p_0, is given by

$$p_0 = \gamma_r \beta_r m_0 c \tag{2.2}$$

where m_0 is the rest mass of the particle. At a given point along the ring, there is a local coordinate system (x, y, z) centered on where an ideal 'reference' particle would be, known as the synchronous particle [6]. The behaviour of a particle is described by the six-dimensional phase space $(x, x', y, y', z, \delta)$ composed of the spatial coordinates and their conjugate momenta (e.g. $x' \doteq dx/ds$ which within the paraxial approximation can be expressed as p_x/p_0) [6]. For our work on space charge and wake fields, we are interested in the longitudinal phase space (z, δ) where z is the longitudinal coordinate in the accelerator s trajectory and δ is the relative momentum offset given by $(p - p_0)/p_0$.

A synchrotron accelerates charged particles which also have their own electromagnetic (EM) field and so the beam particles interact with each other. This develops a collective behaviour because the effect of one particle depends on the global distribution such that the particles oscillate together, changing the beam oscillations. Thus, without attempts of beam

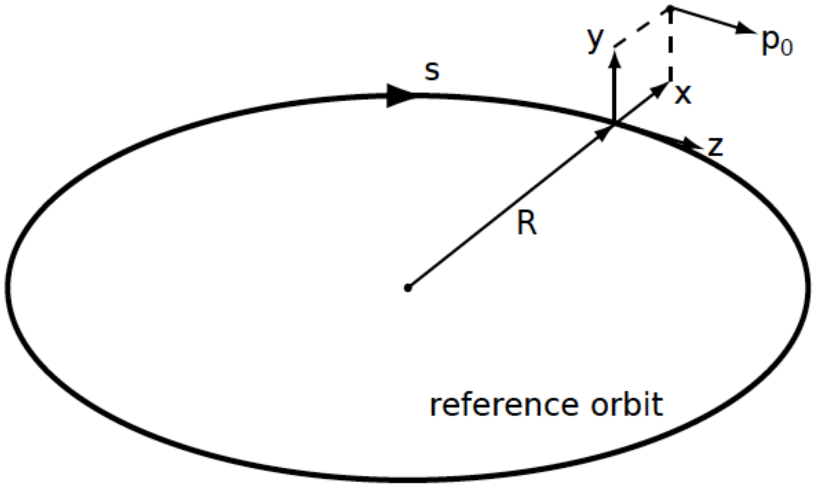

Figure 2.1: This is the Frenet-Serret coordinate system, consisting of a bending radius R of the synchrotron, position along the circumference s of a particle with momentum p_0 and local coordinate system at each point along the orbit of (x, y, z). Courtesy of [7].

confinement, this can lead to instabilities, given by unstable motion where the amplitude of oscillation of the beams increase exponentially in time, eventually hitting the pipe walls [2]. There are many collective effects that contribute to this behaviour which can be grouped into self-induced EM fields, coulomb collisions or EM fields from other charge distributions [8], where space charge and wake fields fall into the first group.

Additionally, we can describe beam particles by the betatron tune that relates their motion through an accelerator by measuring the number of betatron oscillations in one revolution [6], hence a change in this value, the tune shift $\Delta Q_{x,y}$, is a useful quantity to measure the first order perturbation to the transverse dynamics. Similarly, the synchrotron tune, Q_s, refers to the number of longitudinal oscillations performed by the particles in one turn. We can also quantify the size of the beam in the transverse plane, $\sigma_{x,y}$, by the optical β-function and geometric emittance, $\epsilon_{x,y}$, by

$$\sigma_{x,y} = \sqrt{\beta_{x,y}(s)\epsilon_{x,y}} \tag{2.3}$$

for on-momentum particles, travelling with the same momentum as the synchronous particle [6]. The beam size thus also has a contribution of $\delta \times D(s)$, where $D(s)$ is the dispersion function when a particle is travelling with off-momentum such that $\delta \neq 0$.

2.1 Space charge and wake fields

The two collective effects we will be focusing on are space charge and wake fields. Space charge is the EM force between charged particles in a beam and is consequently highly dependent on the number of particles per bunch. It acts like a non-linear lens, defocusing

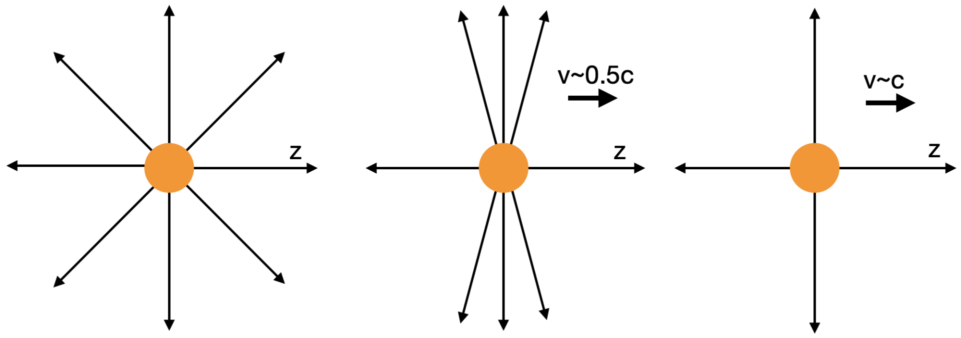

Figure 2.2: Electrostatic field lines for a relativistic positively charged particle at different energies (inspired by [12]).

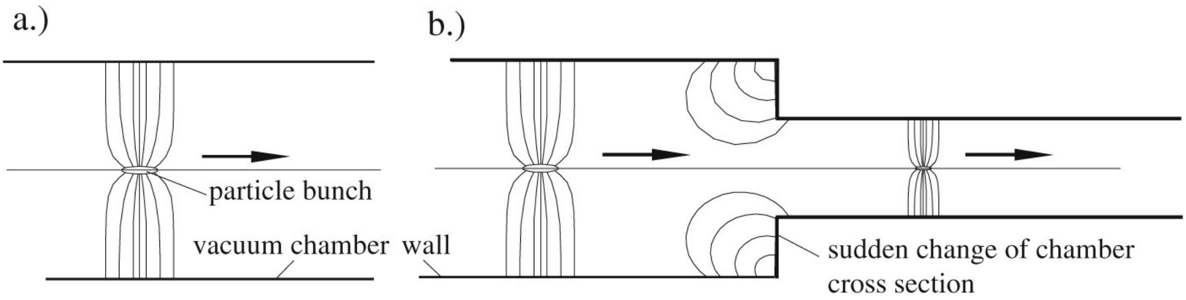

Figure 2.3: Figure a) shows the electric field of a particle bunch moving through a perfectly conducting and smooth pipe, compared to b) which shows the resulting wake fields from a non-uniform pipe. Courtesy of [13].

the beam in the transverse plane [11]. Space charge is produced by the charge distribution of the beam which is also effected by the beam's interaction with the vacuum pipe walls, here assumed to be perfectly conducting and smooth [11]. Particles are accelerated at relativistic energies in an accelerator, which affects the particles' electric field. Figure 2.2 illustrates that the electrostatic field lines of a relativistic charged particle contract in the direction of travel due to Lorentz contraction [12]. As the charge approaches ultra-relativistic energies like in an accelerator, the field lines become confined such that the effect of space charge (force of one charged particle on another in the beam) is only felt at the same longitudinal position.

Meanwhile, wake fields are generated by the finite conductivity of the walls of the pipe and by all its geometric variation in a real pipe [12]: the interaction of the beam with its surroundings. A link between the two effects is shown pictorially in Fig. 2.3. Figure 2.3*a* demonstrates the constrained electric field for a particle bunch moving through a uniform and perfectly conducting pipe with no charge losses. We see that the EM field has a slight spread in angle, not perfectly constrained as this depicts the field in a real machine where the angle depends on $1/\gamma_r$ [13]. We have assumed for this work that the charged particle energy is sufficiently large that $\gamma_r >> 1$. In Fig. 2.3*b* we see a change in the pipe shape, such that the field drags behind the charge, resulting in wake fields being felt by all particles behind the source particle [13]. Wake fields can also be analogously compared to the wake created by a speed boat, where the boat is a charged particle and the resulting wake disturbs the particles in its path. Interestingly, wake dissipation is slow such that the particle that created the wake may also experience it after one turn through the accelerator [2]. Wake fields are thus a source of instability whilst space charge changes the beam dynamics.

2.2 Transverse mode coupling instability

The instability we will be analysing is called transverse mode-coupling instability (TMCI), also known as strong head-tail instability [9]. As indicated by the name, we will be looking at the instability due to coherent tune mode coupling in the transverse plane, as a function of the average longitudinal position and relative momentum offset. An example of a TMCI due to a broad-band resonator wake field is shown in Fig. 2.4. On the x-axis we have the normalised intensity which is a function of the wake field and on the y-axis we have the coherent tune modes. We thus see the resulting real (blue) and imaginary (red) tune shifts for increasing wake field strength. We see two blue lines stemming from coherent tunes of 0 and -1 that join together – these two modes couple – signifying a TMCI. This is further shown by the resulting imaginary coherent tune which emerges due to this instability.

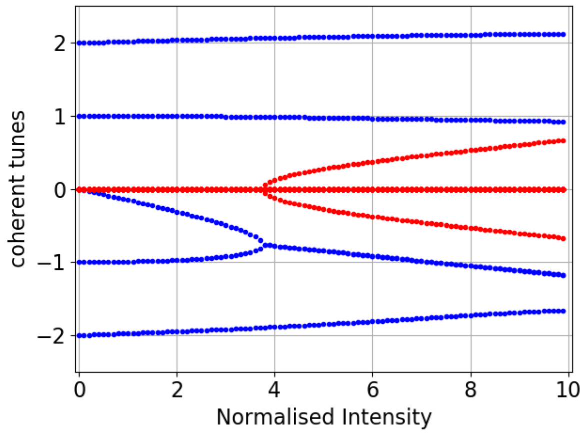

Figure 2.4: Graph showing an example coherent tune mode evolution with increased normalised wake field intensity for a round chamber in order to describe the appearance of a TMCI.

Coherent tune modes can be split into azimuthal and radial modes. Due to the set up of this example plot in Fig. 2.4, we see azimuthal modes -2 to 2 and only one radial mode, where radial modes appear per azimuthal mode. The origin of the coherent tunes, here for zero wake field intensity, signify their azimuthal mode number. The composition of these normal polar modes can be modelled by the standing waves produced at resonant frequencies for a thin vibrating circular membrane, with an infinite number of combinations [10]. The circular membrane is analogous to the beam cross-section in longitudinal phase space. In our model, the transverse beam is divided by rings and slices into many cells. The number of slices corresponds to the number of azimuthal modes and the number of rings corresponds to the number of radial modes exhibited. Hence, the way the transverse beam is composed in our model effects the way the TMCI will be interpreted as it dictates the number of modes considered, with significant changes for increased radial modes.

2.3 BimBim

The code we are using is called BimBim and it simulates two counter-circulating beams in a synchrotron [14]. It is a python implementation of the Circulant Matrix Model (CMM) that calculates the one turn matrix for each beam. The CMM requires a polar composition of the beam in longitudinal phase space, discretised by rings and slices, so that it is composed of many cells as shown in Fig. 2.5.

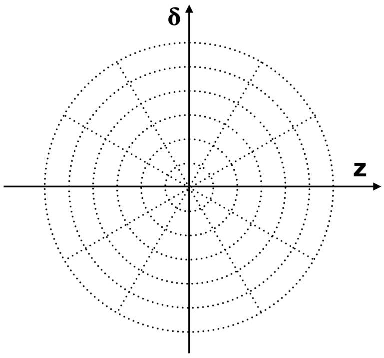

Figure 2.5: Example beam discretisation by rings and slices into cells in longitudinal phase space.

BimBim is already capable of considering the transport of the beams through the lattice of the synchrotron and the effect of coupling wake fields. To model the combined effect of space charge and wake fields we thus needed to add an action module to BimBim that calculates the space charge matrix containing the space charge kicks between all combinations of interacting cells such that the one turn matrix becomes the product of

$$M_{OneTurn} = M_{Lattice} \cdot M_{SpaceCharge} \cdot M_{WakeFields}. \tag{2.4}$$

The action of wake fields or space charge can also be considered separately with the transport lattice. We only considered one beam and one bunch for this work, however this can be scaled up in the future as necessary. BimBim can be used for beam instability work by diagonalising the one turn matrix with the appropriate transport and action modules. Then, calculating the complex eigenvalues, λ, allows the resulting coherent tune modes to be found using [7]

$$Q = i\log(\lambda)/(2\pi), \tag{2.5}$$

where the real part represents real tunes and the imaginary part represents where the real tune modes have coupled, displaying potential sites of instability.

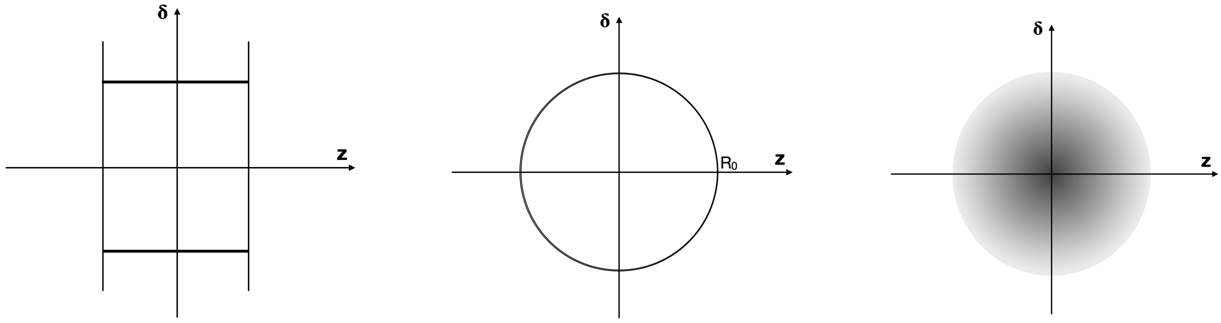

(a) Airbag square-well (b) Airbag (c) Gaussian

Figure 2.6: Beam charge distributions in longitudinal phase space

2.4 Beam distributions

The distributions we will be using to simulate tune shifts are the airbag and Gaussian distributions. A benchmark to our new computational framework is the airbag square-well distribution, which has been a popular way of describing the beam charge distribution. In a square-well potential, the particles are reflected by the walls, where they feel a rebounding force. Applying the confinement due to the airbag model of two infinitely thin paths, we get the distribution in longitudinal phase space shown in Fig. 2.6a, where the particles seem to travel in a square like motion with instant reflection to the opposite δ level.

Similar to the airbag square-well is the airbag distribution in a linear potential, which is a better approximation to the potential generated by RF cavities in an accelerator. This distribution models the beam in longitudinal phase space as an infinitely thin ring of charge, shown in Fig. 2.6b with radius R_0 such that the distribution is given by

$$\Psi(z,\delta) = \begin{cases} \frac{1}{2\pi}, & \text{if } z^2+\delta^2 = R_0^2 \\ 0, & \text{otherwise.} \end{cases} \tag{2.6}$$

The new approach we took was to consider the beam charge distribution in BimBim as a Gaussian. In normalised phase space with standard deviations σ_z and σ_δ (referred to as the rms bunch length and momentum deviation, respectively) the distribution is given by

$$\Psi(z,\delta) = \frac{1}{2\pi\sigma_z\sigma_\delta} e^{-\frac{z^2}{2\sigma_z^2}-\frac{\delta^2}{2\sigma_\delta^2}} \tag{2.7}$$

and represented graphically in Fig. 2.6c. We can see in Fig. 2.6 that space charge will be modelled differently by each distribution as it is dependent on the spread of charge. This also gives us an idea that the Gaussian distribution may be most successful because of its more realistic spread of charge.

Chapter 3

Implementation of Space Charge in BimBim

To make the space charge action module as an input for BimBim so that the one turn matrix considers the effect of space charge, we needed to calculate $M_{SpaceCharge}$, as shown in Eq. 2.4. The space charge matrix calculates the new momentum due to space charge for all interacting cells, hence, it keeps the same positional x value, but for each discretised cell calculates an additional term due to the space charge kick after each turn, k, defined as

$$\begin{bmatrix} x_{1,k+1} \\ x'_{1,k+1} \\ \vdots \\ x_{n,k+1} \\ x'_{n,k+1} \end{bmatrix} = \begin{bmatrix} 1 & 0 & \dots & 0 & 0 \\ A_{1,1} & 1 & \dots & A_{1,n} & 0 \\ \vdots & \vdots & \ddots & \vdots & \vdots \\ 0 & 0 & \dots & 1 & 0 \\ A_{n,1} & 0 & \dots & A_{n,n} & 1 \end{bmatrix} \begin{bmatrix} x_{1,k} \\ x'_{1,k} \\ \vdots \\ x_{n,k} \\ x'_{n,k} \end{bmatrix} \tag{3.1}$$

The size of the matrix is given by $2n$, where n is the product of the number of slices, rings and beams, representing the total number of cells considered:

$$n = N_{slices} \cdot N_{rings} \cdot N_{beams}. \tag{3.2}$$

The matrix shows that we get a momentum kick due to space charge, $\Delta x'$, for momentum equations such as the simplified example $x'_{1,k+1} = \Delta x' + x'_{1,k}$ where $\Delta x' = A_{1,1}x_{1,k}$. We are thus interested in calculating all the possible space charge kicks for a given beam discretisation and want to first construct the space charge interaction matrix which only consists of these values, represented by 'A' constants in $M_{SpaceCharge}$, with the rest zeroes.

In summary, to build the space charge matrix we start with the identity matrix, size-dependent on Eq. 3.2 and add the calculated space charge interaction matrix.

3.1 Derivation of the space charge kick

The space charge kick can be defined as the net change of momentum over one turn, given by $\Delta x' = \Delta p_x/p_0$. First, we want to calculate the space charge kick for one particle, then advance to two particles, and ultimately the kick between two cells of a given beam charge distribution in polar coordinates, to input in the space charge interaction matrix for all combinations of cells.

To derive the space charge kick for one particle, we can start with Newton's II law which states that the rate of change of momentum is equal to the force applied,

$$\frac{d\vec{p}}{dt} = \vec{F}. \tag{3.3}$$

If we linearise the equation we only consider the force close to the beam centroid so that we model the coherent motion of the beam with same frequency particles. Outside the beam centroid, the force becomes non-linear with a spread in particle frequency which can cause Landau damping [15]. Hence, by linearising we recognise that we are looking at the effects of space charge with a pessimistic outlook as we are not considering the possibility of Landau damping suppressing the resulting transverse mode coupling instabilities [15].

The force due to space charge is dependent on the electric field of the charged particle which we assume to be Gaussian. Thus, linearising in x we get the force as [11]

$$F_x = \frac{qE_x}{\gamma_r^2} \tag{3.4}$$

taking into account the charge, q, of the particle. The electric field is represented by a transverse Gaussian charge distribution with standard deviations σ_x and σ_y to get [16]

$$E_x = \frac{1}{2\pi\epsilon_0} \frac{x}{\sigma_{x,y}(\sigma_x + \sigma_y)} \delta(z). \tag{3.5}$$

Significantly, the electric field is constrained in the longitudinal plane as discussed in Sec. 2.1 and shown in Fig. 2.2, because of the relativistic energy of particles in an accelerator. This is the reason for the Dirac delta function with respect to the longitudinal position in z. Now, substituting equations 3.4 and 3.5 into the linearised Eq. 3.3 we get:

$$\frac{dp_x}{dt} = \frac{q}{2\pi\epsilon_0\gamma_r^2} \frac{x}{\sigma_{x,y}(\sigma_x + \sigma_y)} \delta(z). \tag{3.6}$$

We can integrate the electric field over one turn and divide by $\beta_r c$ to get the momentum in x

$$p_x = \frac{q}{2\pi\epsilon_0 c\gamma_r^2\beta_r} \delta(z) \oint \frac{x}{\sigma_{x,y}(\sigma_x + \sigma_y)} \mathrm{d}s. \tag{3.7}$$

Using the smooth approximation that states the optical β function is constant over the ring such that $\sigma_x = \sigma_y$ [16] and substituting in Eq. 2.3 we get

$$p_x = \frac{qC}{4\pi\epsilon_0 m_0 c\gamma_r^2\beta_r\beta\epsilon} x\delta(z) \tag{3.8}$$

with the circumference of the accelerator, C. Hence, to obtain the space charge kick, $\Delta x'$, of a source charge q_s on a witness particle with charge q_w, we consider their respective charges and positions and divide by p_0 using Eq. 2.2:

$$\Delta x' \approx \frac{q_s q_w C}{4\pi\epsilon_0 m_0 c^2\gamma_r^3\beta_r^2\beta\epsilon} (x_w - x_s)\delta(z_w - z_s). \tag{3.9}$$

The optical beta function refers to where the kick is applied. Now if we consider the kick of a cell j on a witness particle, we integrate the kick over its normalised distribution $N\Psi(z_j, \delta_j)$ in phase space area Ω_j, where N is the number of beam particles per bunch. This gives

$$\Delta x'_j(z_w) = A_0(x_w - x_j) \int\limits_{\Omega_j} \mathrm{d}z_j \mathrm{d}\delta_j \Psi(z_j, \delta_j)\delta(z - z_j) \tag{3.10}$$

with constant

$$A_0 = \frac{Nq^2C}{4\pi\epsilon_0 m_0 c^2 \gamma_r^3 \beta_r^2 \beta\epsilon}. \tag{3.11}$$

If we then integrate the kick over a cell i with a phase space area Ω_i and normalise by the mass of the cell so that the force felt by each particle will depend on the size of cell i, we get

$$\Delta x'_{i,j} = A_0(x_i - x_j)\frac{\int_{\Omega_i} \mathrm{d}z_i \mathrm{d}\delta_i \int_{\Omega_j} \mathrm{d}z_j \mathrm{d}\delta_j \Psi(z_i, \delta_i)\Psi(z_j, \delta_j)\delta(z_i - z_j)}{\int_{\Omega_i} \mathrm{d}z_i \mathrm{d}\delta_i \Psi(z_i, \delta_i)}. \tag{3.12}$$

The CMM requires a polar decomposition of the beam in phase space so we apply the transformation in normalised polar coordinates

$$\begin{aligned} z_i &\longrightarrow r_i\sigma_z \cos(\theta_i) \\ \delta_i &\longrightarrow r_i\sigma_\delta \sin(\theta_i) \\ z_j &\longrightarrow r_j\sigma_z \cos(\theta_j) \\ \delta_j &\longrightarrow r_j\sigma_\delta \sin(\theta_j) \end{aligned}$$

where the Jacobian of the transformation is $r_i r_j \sigma_z^2 \sigma_\delta^2$, so we get the kick in normalised polar coordinates:

$$\Delta x'_{i,j} = A_0(x_i - x_j) \int\limits_{\Omega'_i} \mathrm{d}r_i \mathrm{d}\theta_i \int\limits_{\Omega'_j} \mathrm{d}r_j \mathrm{d}\theta_j r_i r_j \sigma_z^2 \sigma_\delta^2 \Psi(r_i\sigma_z \cos(\theta_i), r_i\sigma_\delta \sin(\theta_i))$$
$$\Psi(r_j\sigma_z \cos(\theta_j), r_j\sigma_\delta \sin(\theta_j))\delta(K_0(r_i, \theta_i, r_j, \theta_j)) \; / \int\limits_{\Omega'_i} \mathrm{d}r_i \mathrm{d}\theta_i \Psi(r_i\sigma_z \cos(\theta_i), r_i\sigma_\delta \sin(\theta_i)). \tag{3.13}$$

The argument of the Dirac delta function is given by

$$K_0(r_i, \theta_i, r_j, \theta_j) = r_i\sigma_z \cos(\theta_i) - r_j\sigma_z \cos(\theta_j), \tag{3.14}$$

where it can be simplified using the identity

$$\delta(\alpha x) \equiv \frac{1}{|\alpha|}\delta(x), \tag{3.15}$$

such that we can re-define the constant

$$A = \frac{A_0}{\sigma_z} = \frac{Nq^2C}{4\pi\epsilon_0 m_0 c^2 \gamma_r^3 \beta_r^2 \beta\epsilon\sigma_z} \tag{3.16}$$

and the argument becomes

$$K(r_i, \theta_i, r_j, \theta_j) = r_i \cos(\theta_i) - r_j \cos(\theta_j). \tag{3.17}$$

Additionally, for the Gaussian distribution we replace Eq. 2.7 by the equivalent in normalised polar coordinates

$$\Psi_G(r, \theta) = \frac{r}{2\pi} e^{-\frac{r^2}{2}} \tag{3.18}$$

and for the airbag distribution in polar coordinates the distribution in Eq. 2.6 becomes

$$\Psi_{AB}(r, \theta) = \frac{1}{2\pi} \delta(r - R_0). \tag{3.19}$$

Thus, the space charge kick of a cell j on i given in polar coordinates for polar distributions Ψ_P is:

$$\Delta x'_{i,j} = A(x_i - x_j) \frac{\int_{\Omega'_i} dr_i d\theta_i \int_{\Omega'_j} dr_j d\theta_j \Psi_p(r_i, \theta_i) \Psi_p(r_j, \theta_j) \delta(K(r_i, \theta_i, r_j, \theta_j))}{\int_{\Omega'_i} dr_i d\theta_i \Psi_p(r_i, \theta_i)}. \tag{3.20}$$

3.2 Discretisation

Having found the kick due to space charge of a cell j on i in Eq. 3.20, we adapted the calculation for numerical implementation. We needed to discretise the integrals with the standard formula [10]

$$\int_a^b f(y) \mathrm{d}y = \lim_{\Delta y \to 0} \sum_{y=a}^{b} f(y) \Delta y \tag{3.21}$$

and approximate the Dirac delta function to a rectangular function, $\Pi(y)$,

$$\int f(y) \delta(y - y_i) \mathrm{d}y = f(y_i) \approx \lim_{\Delta y \to 0} \sum f(y_i) \Pi(y - y_i) \Delta y. \tag{3.22}$$

This then gives the numerical space charge kick as

$$\Delta x'_{i,j} = A(x_i - x_j) \frac{\sum\limits_{r_i, \theta_i, r_j, \theta_j} \Psi_p(r_i, \theta_i) \Psi_p(r_j, \theta_j) \Pi(K(r_i, \theta_i, r_j, \theta_j)) \Delta z \Delta r_i \Delta \theta_i \Delta r_j \Delta \theta_j}{\sum\limits_{r_i, \theta_i} \Psi_p(r_i, \theta_i) \Delta r_i \Delta \theta_i}. \tag{3.23}$$

We let cells i and j be integrated with the same step sizes, such that $\Delta r_i = \Delta r_j$ and $\Delta \theta_i = \Delta \theta_j$, meaning that the computed kick only depends on the three parameters Δz, Δr and $\Delta \theta$. Instead of working with the step size we were summing over, we decided to work with the parameters as functions of number of steps summed over, so we will refer to them from now on as N_Z, N_θ and N_R. The next step was thus to find the appropriate number of steps which compromised on computation speed and accuracy of the true integral – finding the convergence of the parameters. The parameters to be optimised are shown graphically in Fig. 3.1b for the Gaussian distribution, as well as displaying the cell discretisation of an

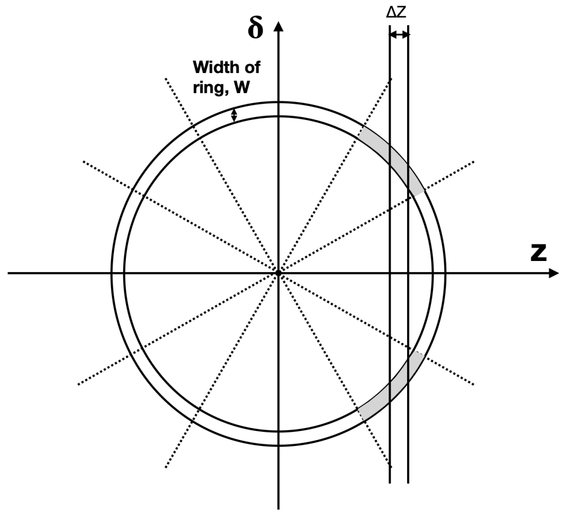

(a) Airbag distribution

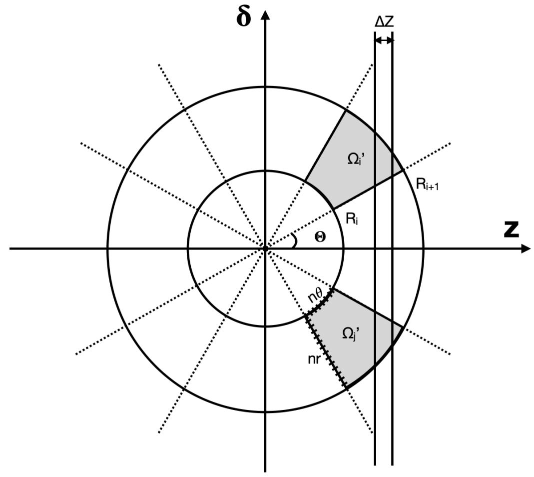

(b) Gaussian distribution

Figure 3.1: Charge distributions in longitudinal phase space adapted for numerical computation by discretisation.

example 2 rings and 12 slices. The figure shows how there are two cells that interact at a time, with an example two cells highlighted in grey, with the combination of the interacting pairs restricted by the constraint of falling within the width of Δz (which corresponds to $1/N_Z$).

In order to apply the same numerical scheme to the airbag distribution, we also had to approximate the infinitely thin ring to a ring of finite width W, such that the distribution in Eq. 3.19 becomes

$$\Psi_{AB}(r,\theta) = \begin{cases} \frac{1}{2\pi W}, & \text{if } (R_0 - W/2) < r < (R_0 + W/2); \\ 0, & \text{otherwise.} \end{cases} \tag{3.24}$$

The computation of the airbag distribution for a finite width is shown in Fig. 3.1a for an example 12 slices. Hence, as well as optimising the number of steps N_R, N_θ and N_Z, for the airbag distribution we also needed to optimise the width of the ring, W.

3.3 Method of convergence

Converged parameters of N_R, N_θ and N_Z were found for the airbag with 20 slices and 1 ring for decreasing ring width until we found the converged width. For the Gaussian distribution we found the converged parameters for increasing number of rings and slices, starting with 20 slices 1 ring, 20 slices 10 rings and then increasing by 20 slices and 10 rings each time to see if we could reach a converged number of rings and slices.

To find the converged parameters N_Z, N_θ and N_R, we worked with the space charge interaction matrix that only considers the computed space charge kicks. The convergence

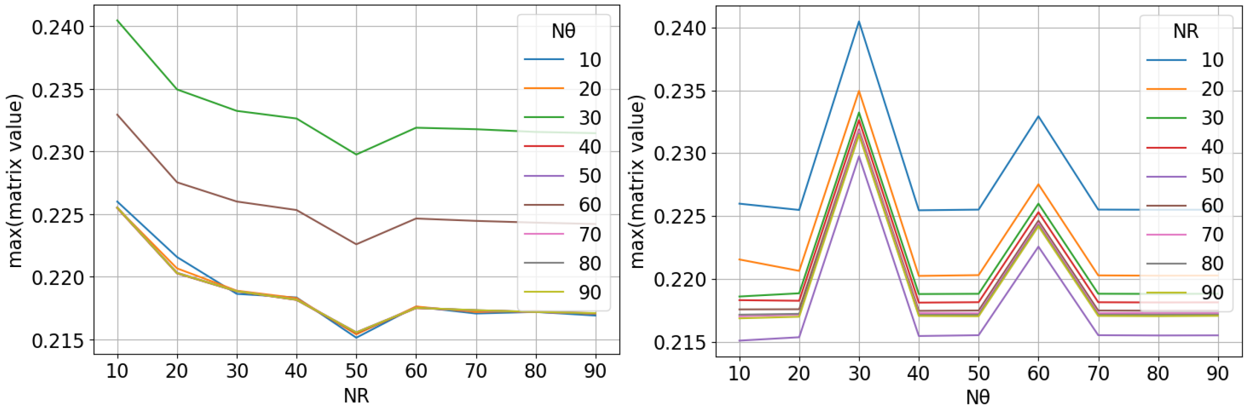

(a) N_θ vs max interaction matrix value for different values of N_R

(b) N_R vs max interaction matrix value for different values of N_θ

Figure 3.2: Graphs for airbag distribution of width 0.1 for 20 slices for N_Z=10

was tested on the maximum force due to space charge which is the maximum space charge interaction matrix value. We started by finding the converged values of N_R and N_θ for increasing N_Z, where doubling N_R or N_θ changed the maximum matrix value by less than 1%. We then checked by doubling N_Z with converged N_R and N_θ if the maximum matrix value changed by less than 1%, until this was the case.

3.3.1 Convergence of parameters for the airbag distribution

An example calculation for the convergence of N_Z, N_θ and N_R can be done for the airbag distribution with width 0.1 for 20 slices and a necessary 1 ring. We started by doing a rough scan for $N_Z = 10$ and plotted the maximum value of the interaction matrix for N_θ and N_R between 10 and 100 in steps of 10, respectively, as shown in Fig. 3.2. From these, we gained an idea of which values to test for doubling to see if the maximum interaction matrix value changed by less than 1%. The various peaks on the graphs are due to resonance and so we knew not to choose these values. We found $N_\theta = 80$ and $N_R = 70$ here.

We then checked that these values of N_θ and N_R were also converged for increasing N_Z by using the same method of checking by doubling. Starting from $N_Z = 10$, we increased by intervals of 10 and for each checked that if it was doubled whether the maximum space charge interaction matrix value changed by less than 1%, until this was the case. We got the converged N_Z value to be 30. We also plotted N_Z against the maximum matrix values so that we could visually check that our converged N_Z was appropriate and not an anomaly.

We repeated this process for widths of 0.01 and 0.001. However, for the width of 0.001 we were unable to find a converged value for the maximum space charge interaction matrix value as it was too numerically demanding. This behaviour was confirmed by theory that the value diverges as the width tends to zero [17]. As we wanted to find the thinnest ring width computationally possible within a reasonable time limit, we chose to test the width of 0.005, where we were successful in finding the converged parameters N_Z, N_θ and N_R. The width

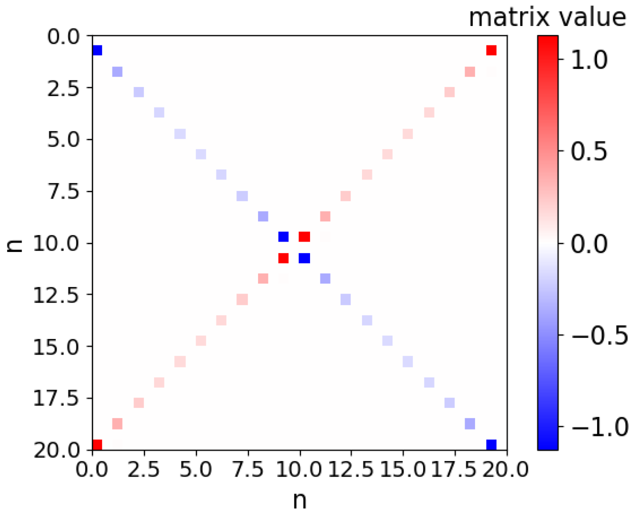

Figure 3.3: Visual representation of the space charge interaction matrix for $n = 20$ cells for converged parameters of an airbag distribution of width 0.005, colour dependent on the matrix value.

of 0.005 and its converged parameters is what we will be using in our future analysis. Table 3.1a shows the converged parameters we found for this work with an airbag distribution of 20 slices.

There are several ways to check that our chosen width of 0.005 is an appropriate choice, where one can be done by looking at a visual representation of the space charge interaction matrix for its converged parameters. This is shown in Fig. 3.3, color coded dependent on the matrix value. We can see that the non-zero values are where we expect them to be, as we see that when grouping the cells into squares of 4 elements, the non-zero values are on the bottom left, as confirmed by the placement of '$A_{i,j}$' values in Eq. 3.1. We only see non-zero values along the diagonals and zeroes surrounding them. This is because we are only considering 1 ring as this is for the airbag distribution. We can remind ourselves of the set-up in Fig. 3.1a which shows only a pair of cells interacting. Remembering the constraint that space charge forces only act on cells in our model at the same longitudinal z, we want a ring width that is small enough so that the cells only feel the force of one other, hence we want the space charge kicks to be confined to the diagonals of the matrix. From Eq. 3.2 we expect our axes to vary from 0 to $20 \times 1 \times 1$ and this is why we see values of opposite magnitude in pairs, denoted by n and $20 - n$. For a beam discretisation with more than 1 ring for the Gaussian distribution, we expect the matrix to have more values of interaction as each cell will interact with several others.

3.3.2 Convergence of parameters for the Gaussian distribution

With the same method we calculated the converged parameters for the Gaussian distribution, varying the number of rings and slices compared to varying the ring width for the airbag distribution. These parameters are shown in Tab. 3.1b. We only managed to find

Width	N_Z	N_θ	N_R
0.1	30	80	70
0.01	130	80	70
0.005	230	70	80

(a) Airbag distribution of 20 slices and 1 ring

N_{slices}	N_{rings}	N_Z	N_θ	N_R
20	1	50	80	50
20	10	160	70	20
40	20	350	70	40

(b) Gaussian distribution

Table 3.1: Converged parameters

the converged parameters up to a beam discretisation determined by 40 slices and 20 rings. Above 40 slices our method of convergence was very numerically demanding with long computational times of more than 30 days for the computation of one space charge interaction matrix. This meant that we were not able to obtain the converged parameters for desired beam discretisations of 60 slices 30 rings and 80 slices 40 rings. This means that we can't determine a converged number of rings and slices, where increasing their number would not affect any change in our TMCI analysis.

Chapter 4

Space Charge Tune Shift Analysis

Having found the converged parameters, we next wanted to look at how the space charge tune shift varies for the three distributions: analytical airbag square-well and simulated airbag and Gaussian. This was done by comparing the coherent tune for the distributions, plotted against the theoretical space charge tune shift (the space charge parameter).

The theoretical space charge tune shift for a particle passing through the accelerator is given by [7]

$$\Delta Q_x^{sc}(z) = \frac{q\lambda(z)}{8\pi^2\epsilon_0\beta_r\gamma_r^2 p_0 c}\oint \mathrm{d}s \frac{\beta_x(s)}{\sigma_x(s)(\sigma_x(s)+\sigma_y(s))}. \tag{4.1}$$

Similar to the calculation of the space charge kick in Sec. 3.1, we can compute the maximum theoretical space charge tune shift reached at $z = 0$ by using the smooth approximation and substituting in equations 2.2 and 2.3 such that we get

$$\Delta Q_{sc}(z=0) = \frac{q\lambda(z=0)C}{16\pi^2\epsilon_0 m_0 c^2\beta_r^2\gamma^3\epsilon} \tag{4.2}$$

with the line density of the bunch,

$$\lambda(z=0) = \frac{qN}{\sqrt{2\pi}\sigma_z}. \tag{4.3}$$

We can also link the theoretical space charge tune shift to our constant A in Eq. 3.16 from the derivation of the space charge kick such that we have

$$\Delta Q_{sc}(z=0) = \frac{A}{4\pi}\frac{\beta}{\sqrt{2\pi}}. \tag{4.4}$$

To conveniently apply these results to any machine, we divided by the synchrotron tune, Q_s, such that we get the normalised theoretical space charge tune

$$Q_{sc}^{theor} = \frac{\Delta Q_{sc}}{Q_s}. \tag{4.5}$$

We can calculate the simulated space charge tune shifts for the airbag and Gaussian distributions using Eq. 2.5. We take the real part and again divide by the synchrotron tune to get our simulated space charge tune shifts in units of Q_s:

$$Q_{sc}^{sim} = \frac{\Delta Q}{Q_s} = \frac{Re(i\log(\lambda))}{2\pi Q_s}. \tag{4.6}$$

As a benchmark to our model we compare the simulated tunes for the airbag model with the airbag square-well, which has its normalised analytical spectrum given by [7]

$$\frac{\Delta Q_{n_a}}{Q_s} = -\frac{Q_{sc}^{theor}}{2} \pm \sqrt{\left(\frac{Q_{sc}^{theor}}{2}\right)^2 + (n_a)^2} \tag{4.7}$$

for azimuthal modes n_a.

As mentioned in Sec. 2.2, there are two types of tune shift modes: azimuthal and radial. Since the azimuthal modes depend on the number of slices and the radial modes depend on the number of rings, the airbag distribution considers 20 azimuthal modes and only 1 radial mode, whilst the Gaussian distribution can consider multiple radial modes as it can consider more than 1 ring.

4.1 Airbag vs airbag square-well

First, we wanted to compare our numerical tune shifts for the airbag to the analytical spectrum for the airbag square-well. In Fig. 4.1 we plotted the theoretical space charge tune shift, given by Eq. 4.5, against the simulated coherent tune, given by Eq. 4.6, both in units of synchrotron tune. We did this for two different airbag widths 0.005 (blue) and 0.01 (red), for increasing space charge parameter by increasing the number of beam particles per bunch. We plotted the tune shifts for two widths in order to compare the effect of the ring width and as a second check that the width of 0.005 is appropriate for future analysis. We can also compare if tune shifts produced for one of the widths match the analytical airbag square-well spectrum better, given by Eq. 4.7.

Comparing the tune shifts produced by the different airbag widths we can see that for the smaller width of 0.005, the high order negative azimuthal modes -10 and -9 decrease more strongly, which is a result of the diverging matrix term, expected in the theory for the airbag for decreased ring width [17]. The decrease in width has otherwise not seemed to produce a significant change in tune shifts. Modes 1 and 2 for the larger width of 0.01 go to zero faster than 0.005, meaning the tune shift values are closer to theory for the decreased width for higher space charge. It is clear that the width of 0.005 is a sufficient choice due to its likeness to theory and the sign that decreasing the width would not lead to a significant improvement in the accuracy of the tune shifts, which would also be more numerically demanding.

Comparing the airbag model of width 0.005 to the analytical spectrum for the airbag square-well model, we see that when the theoretical space charge tune is equal to zero, the simulated and analytical coherent tunes match, confirming that the space charge matrix is the identity matrix at the origin since there are no space charge kicks. From here, the

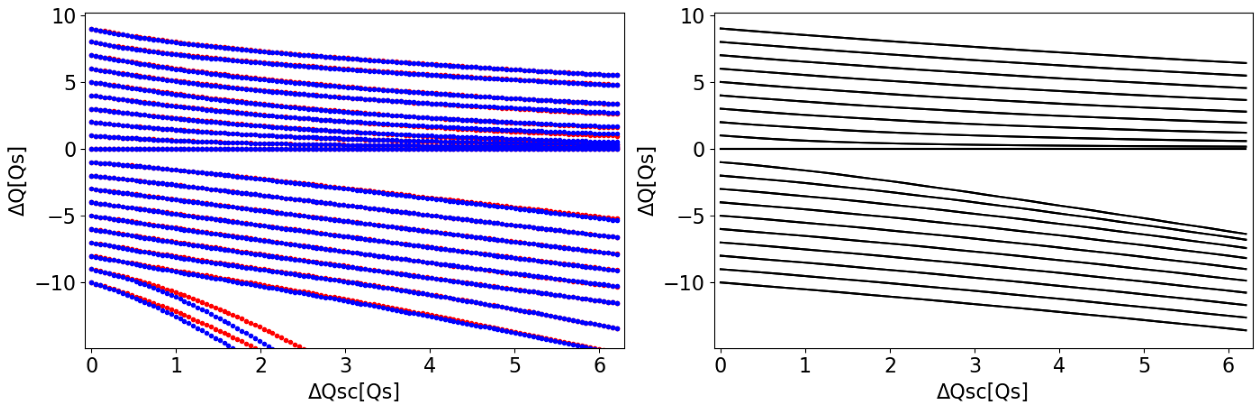

Figure 4.1: Left: evolution of tune shifts for increasing space charge parameter for airbag model of widths 0.01 (red) and 0.005 (blue). Right: analytical spectrum of tune shifts for airbag square-well model for increasing space charge parameter.

tunes do not follow the theory perfectly, but they follow the same trend that the positive tunes tend to zero and the negative modes tend to negative infinity. This difference can partly be attributed to the fact that the analytical spectrum assumes both an airbag model and a square-well potential, whilst the simulated tune shifts consider an airbag in a linear potential. The simulated positive modes also seem to pair at high space charge strength such as modes 9,8 and 7,6, which does not compare to theory. This behaviour could be a result of our numerical computation such as the approximations of our converged parameters, using a finite ring width and only having 20 slices.

For our purposes, since we simply wanted to check that our method of computation was comparable to theory and we see a similar trend of tune shift modes, we can justify that our computational framework is appropriate for further investigative work with other distributions.

4.2 Airbag vs Gaussian

Next, we wanted to compare how the coherent tune behaved for increasing space charge for the two distributions airbag and Gaussian. First, in Fig. 4.2 we plotted the airbag model (red) and the equivalent configuration for the Gaussian distribution (blue) of 20 slices and 1 ring to get the left graph and only the Gaussian distribution in the right. We can see that the two distributions have different coherent tune mode evolution with increased space charge as the two colours are seen clearly for the positive modes. A difference was expected and can be attributed to their distinct distributions, referring again to Fig. 3.1. We can see that the tune shifts produced for the Gaussian distribution also match the theory at the origin and follow the same general trend as the analytical spectrum. We can see that for the Gaussian distribution, the modes -10 and -9 don't diverge, but we see that for the evolution of tune shift mode 1 and 2, they cross mode zero when space charge is increased, unlike for the converged airbag. This is a new result where the positive modes head downwards,

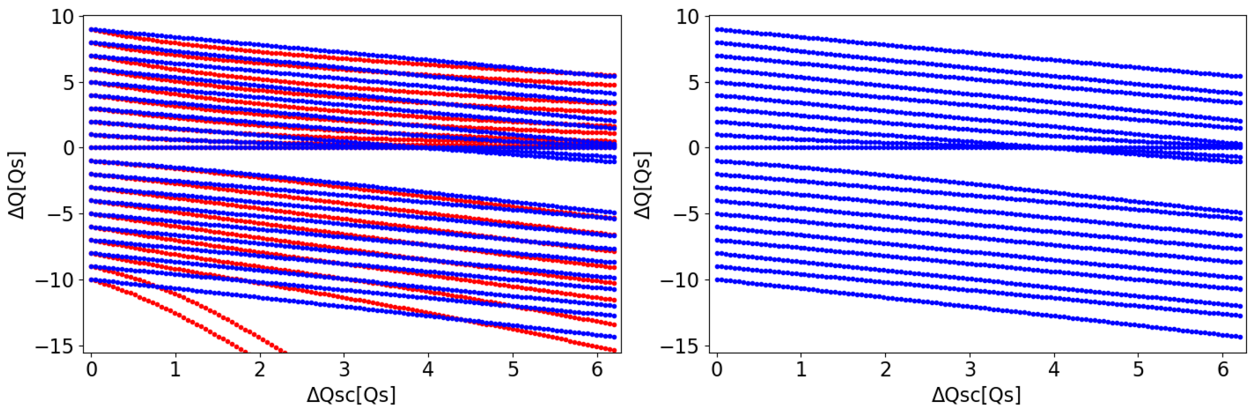

Figure 4.2: Left: Tune shift evolution for airbag of width 0.005 (red) vs Gaussian (blue) distribution of 20 slices 1 ring for increasing space charge parameter. Right: Gaussian only.

crossing mode 0 rather than converging at 0. There also remains the same behaviour of the positive modes bunching in twos at high space charge.

If we increase the number of radial modes for the Gaussian distribution to 10 so that we have a beam discretisation of 20 slices and 10 rings, we get the real coherent modes (pink) in Fig. 4.3, where the tune shifts due to 1 ring (blue) is overlaid as a reference. This is a key difference between the Gaussian and airbag distributions that the Gaussian distribution is capable of considering radial modes since for 1 ring we consider all azimuthal modes but only the radial mode 0. With 10 rings we get 10 radial modes per azimuthal mode. At the origin, the radial modes are not visible since they are degenerate without space charge. As space charge increases, the degeneracy is lifted and multiple radial modes start to appear and drift apart as they gain a spread in frequency. This also leads to the radial modes crossing, which may lead to coupling instabilities later when the wake fields are considered. Again, we see the positive modes to have a downward trend, going below a coherent tune of 0.

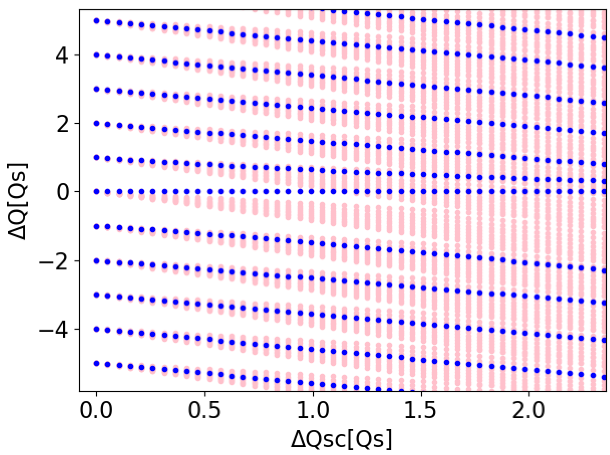

Figure 4.3: Tune shifts plotted as a function of the space charge parameter for the Gaussian distribution with 20 slices and 10 rings (pink) overlaid with the beam discretisation of 20 slices 1 ring (blue).

Chapter 5

TMCI due to Space Charge and Wake Fields

To get the main results of this project, we analysed the TMCI for coherent tunes due to varying space charge forces and wake fields. The one turn matrix now considers both the matrix conveying the behaviour of wake field coupling and the space charge matrix, like in Eq. 2.4. The resulting coherent tunes were calculated by taking Eq. 2.5 and dividing by the synchrotron tune.

First, we need to introduce how we approached plotting the wake fields. We looked at a broadband resonator wake which can be described by several properties. We plotted the wake fields as a function of their normalised intensity given by [18]:

$$I_{norm} = \frac{Nq^2}{2\gamma m_0 \omega_\beta \omega_s C} \times \frac{\omega_r^2 R_t}{Q\overline{\omega_r}}. \tag{5.1}$$

The new variables introduced here are ω_β, ω_s, ω_r the angular frequency of the transverse betatron, of the synchrotron and resonance of the broad-band resonator wake. We also have R_t the so-called shunt impedance, Q the quality factor and $\overline{\omega_r} = \omega_r\sqrt{1 - 1/(4Q^2)}$ [18]. Another useful property is κ, which is used to describe the geometry of the beam pipe and is given by

$$\kappa = \frac{D(z)}{W_x(z)} \tag{5.2}$$

where $D(z)$ is the detuning quadrupolar wake field strength and $W_x(z)$ is the driving dipolar horizontal wake field [18]. We chose to set $\kappa = 0$ such that it represents a round chamber. We also have the parameter $f_r\tau_b$ which is the product of the resonant frequency of the resonator, $f_r = \omega_r/(2\pi)$, and the bunch length, τ_b. This is a useful quantity to compare results with because when we vary $f_r\tau_b$, the normalised intensity of the TMCI threshold varies as shown in Fig. 5.1. The analytical BimBim simulated plot shows there are three distinct sections which we will use as a reference when choosing which $f_r\tau_b$ to use since they dictate which modes couple with each other [18]. For $f_r\tau_b$ between 0 and 1.5, between 1.5 and 2.5 and between 2.5 and 3 we expect different mode coupling regimes.

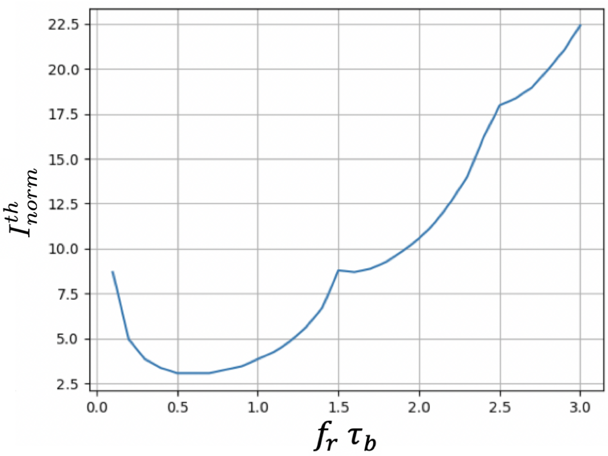

Figure 5.1: Analytical BimBim simulation of $f_r\tau_b$ against the normalised intensity TMCI threshold due to wake fields of a broad-band resonator, courtesy of [18].

Furthermore, this work is generic to any machine with the assumptions that the wake field can be modelled as a broadband resonator and that the vacuum chamber is round. We tested for $f_r\tau_b$ equal to 1, 2 and 3, corresponding to three different types of mode coupling. We did this for both the airbag distribution and the Gaussian distribution in order to compare their expected TMCI thresholds for the interaction of space charge and wake fields. This was done by doing a contour plot of the maximum imaginary coherent tune for varying space charge parameter and wake field normalised intensity.

5.1 TMCI for an airbag distribution

Starting by setting $f_r\tau_b$ equal to one, we get the contour plot of the maximum imaginary coherent tune for varying space charge and wake field strength in Fig. 5.2. We did this because as discussed in Sec. 2.2, when there is transverse mode coupling there results imaginary tune, reflecting the presence of an instability. Hence, plotting the maximum imaginary tune shows us where we expect regions of instability, where dark blue is stable with no imaginary tune and yellow is where the strongest imaginary tune is. In Fig. 5.2 there are three main regions: (1) the yellow top left corner of instability, (2) the dark blue stable triangular region in the middle and (3) the blue top right corner of low imaginary coherent tune.

If we go along the normalised intensity axis for zero space charge, we get the behaviour of the coherent tunes for increasing wake field strength only, shown in Fig. 5.3a. The blue lines represent real coherent tune modes and the red lines represent imaginary modes. As predicted by the contour plot, we see that the imaginary tune shifts become non-zero at a normalised intensity of 3.2 – the TMCI threshold. This is a result of the real modes 0 and -1 coupling, causing two symmetric branches of modes with imaginary tune to emerge.

We can see in Fig. 5.2 from looking at the edge of region (1) that space charge lifts

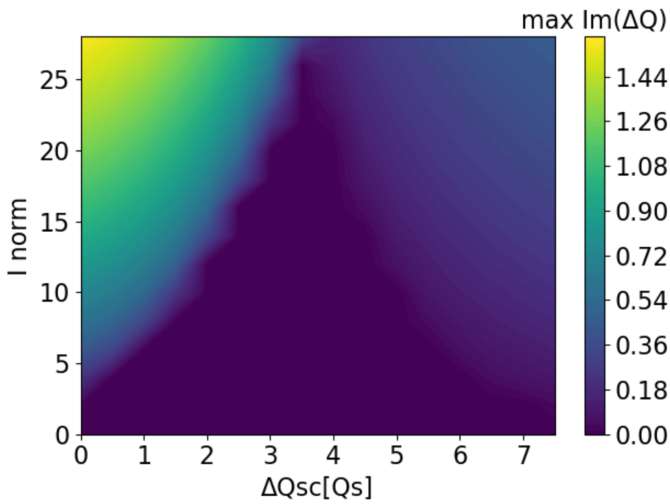

Figure 5.2: Contour plot of the maximum imaginary coherent tune for theoretical space charge tune shift against wake field normalised intensity for an airbag distribution of width 0.005. We assume a broad-band resonator wake field and a round chamber such that $\kappa = 0$, setting $f_r\tau_b = 1$.

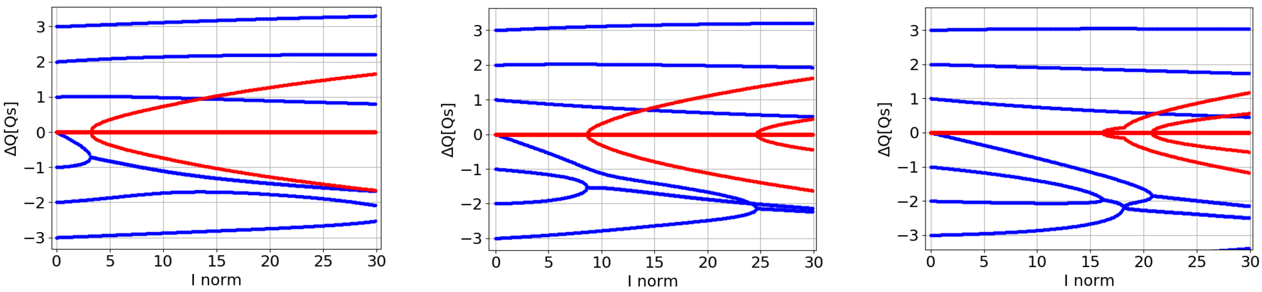

(a) $f_r\tau_b = 1$ (b) $f_r\tau_b = 2$ (c) $f_r\tau_b = 3$

Figure 5.3: Real (blue) and imaginary (red) coherent tunes for increasing wake field normalised intensity for Airbag distribution – comparing TMCI for increasing $f_r\tau_b$.

the TMCI threshold, until we reach a space charge strength of 3.7, where it has completely suppressed the instabilities due to our maximum normalised intensity wake field. Wake fields cause instabilities, whilst as seen in our previous work on space charge, taking Fig. 4.1 as an example, there is no coupling and thus no imaginary tune shifts due to space charge. This behaviour is also reflected in Fig. 5.2 for zero normalised intensity, along the theoretical space charge axis, where the imaginary tune shifts are zero. Region (2) has no presence of imaginary tune shifts and thus is the stable region. This shows us where we want the levels of space charge and wake fields to be in order to keep the beam stable during operation.

Region (3) in Fig. 5.2 reintroduces instabilities after space charge has suppressed the previous instabilities caused by wake fields, so it is now to determine whether this is a true region of instability caused by increased space charge strength or a product of our numerical computation. We can examine this behaviour by taking a constant wake of $I_{norm} = 25$ and varying space charge for airbag widths of 0.1, 0.01 and 0.005, such that we test the effect of

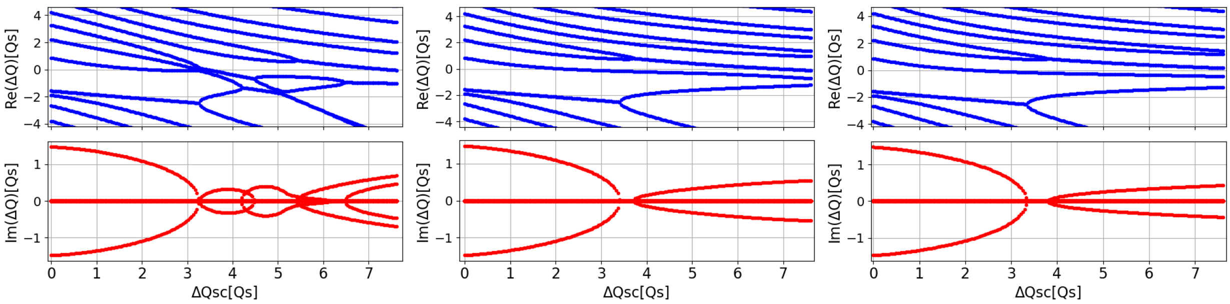

(a) W=0.1 (b) W=0.01 (c) W=0.005

Figure 5.4: Real (blue) and imaginary (red) coherent tunes due to varying space charge and wake fields of $I_{norm} = 25$ with $f_r\tau_b = 1$ for decreasing ring width (a)-(c).

the airbag width on instability regions (1) and (3). We can see in Fig. 5.4 the resulting real (blue) and imaginary (red) coherent tune for decreasing airbag width. We can confirm that region (1) is caused by wake fields as we see the modes 0 and -1 decouple at approximately the same space charge strength of 3.4 in all three plots, showing it is independent of the width. The small variation in values for the different airbag widths can be attributed to their convergence, as the width of 0.1 is far from converged, whilst as we saw in Fig. 4.1 there is not a lot of difference between widths 0.01 and 0.005. Region (3) seems dependent on the airbag width as the plots all vary in space charge strength needed for positive mode coupling, especially for the larger width of 0.1 where we see several extra positive mode couplings occurring. If we focus on modes 2 and 3, we see they require a higher space charge strength for decreasing airbag width, reflecting a reduction in the numerical artefacts of our computation. Significantly, by using an analytical method for the computation of the space charge matrix for an airbag of infinitely thin width, it was confirmed that the instabilities in region (3) vanish [17].

Now, if we want to look at the behaviour for increased $f_r\tau_b$ equal to 2 and 3, we can again produce contour plots of their maximum imaginary coherent tune as a function of space charge and wake field strength, to find three similar distinct regions like in Fig. 5.2 for $f_r\tau_b = 1$. We can again examine the regions of instability by looking at Fig. 5.3 where we have plotted the real and imaginary coherent tune for increasing wake field strength for $f_r\tau_b$ equal to 2 and 3, as well as the previously mentioned $f_r\tau_b = 1$. We can see that increasing $f_r\tau_b$ increases the TMCI threshold from a normalised intensity of 3.2 to 8.6 to 16.2. Hence, a stronger wake field is needed to cause mode coupling for increased $f_r\tau_b$. In Fig. 5.3b for $f_r\tau_b = 2$, we see the coupling of modes -1 and -2 at the TMCI threshold. There is an additional mode coupling at $I_{norm} = 24.4$, however we are only interested in the first coupling as this is the instability that grows the fastest and consequently dominates the beam dynamics. In Fig. 5.3c for $f_r\tau_b = 3$, we observe a more complicated set of mode couplings, between mode -1 and -2, then 0 and -3. Hence, as expected by theory in Fig. 5.1, we see three different regimes of mode coupling for $f_r\tau_b$ equal to 1, 2 and 3.

To compare region (3) of imaginary coherent tune due to the finite airbag width for

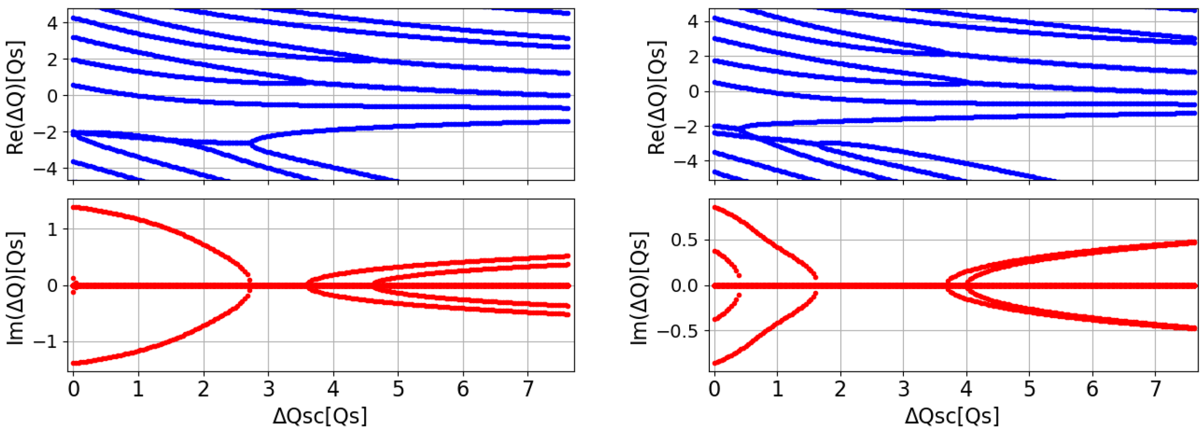

(a) $f_r\tau_b = 2$ (b) $f_r\tau_b = 3$

Figure 5.5: Real (blue) and imaginary (red) coherent tunes for airbag distribution due to fixed wake fields of $I_{norm} = 25$ and varying space charge parameter.

varying $f_r\tau_b$, we set the wake field to have a normalised intensity of 25 and varied the space charge to get the plots in Fig. 5.5 for $f_r\tau_b$ equal to 2 and 3. Increasing $f_r\tau_b$ alters the real negative modes that couple, increasing the TMCI as the real modes decouple at a lower theoretical space charge tune shift. However, the first positive mode coupling of modes 2 and 3 at a space charge strength of 3.6 doesn't change for increased $f_r\tau_b$, showing that it is not caused by the wake field but due to our numerical calculation – not a valid TMCI. The increased $f_r\tau_b$ results in more positive modes coupling, like for $f_r\tau_b$ equal to 2 and 3 which have the additional coupling of modes 4 and 5. This shows that an increased $f_r\tau_b$ amplifies our approximation of a finite width (still noting that the first oscillating mode is most significant and that has not changed). Lastly, increasing $f_r\tau_b$ has thus increased the area of the region of stability (2).

In conclusion of this analysis on the TMCI threshold for the airbag distribution, we have two main findings. An increase in $f_r\tau_b$ leads to an increase in the TMCI threshold due to wake fields and as space charge increases, the TMCI threshold is also increased until the space charge suppresses the mode coupling produced by the wake fields. Both these findings are in agreement with existing theories [4]. However, for our numerical model, there are additional positive mode couplings for increased space charge, produced due to our assumption of a finite width of the airbag, and so should not be considered when determining the TMCI threshold, notably for lower normalised intensity ranges.

5.2 TMCI for a Gaussian distribution

First, keeping the number of azimuthal modes and radial modes the same as for the airbag distribution with 20 slices and 1 ring, we obtained the contour plot of maximum imaginary tune for varying space charge and wake field strength of $f_r\tau_b = 1$ for a Gaussian distribution, shown in Fig. 5.6. We see that the left half of the contour plot looks similar to the corre-

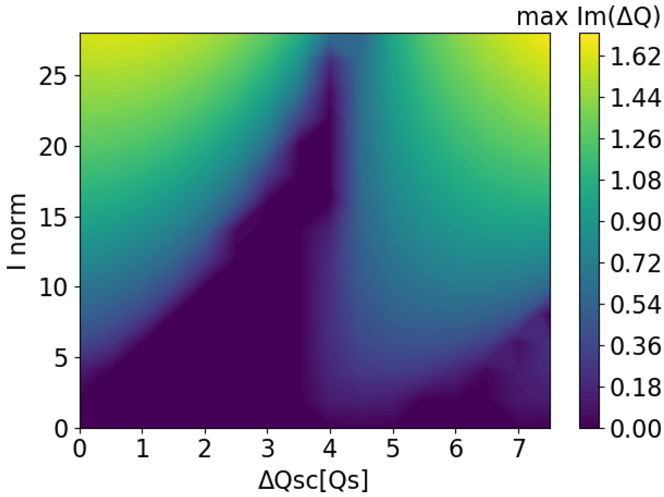

Figure 5.6: Contour plot of the maximum imaginary tune shift for theoretical space charge tune shift against normalised wake field intensity of $f_r\tau_b = 1$ for a Gaussian distribution of 20 slices 1 ring.

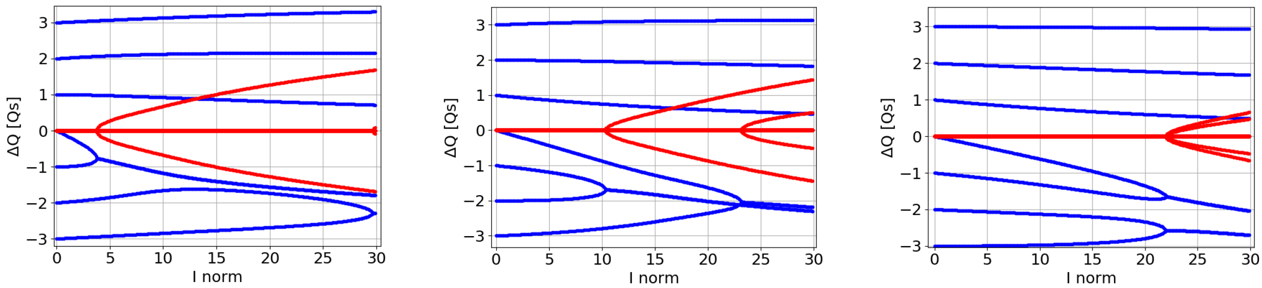

(a) $f_r\tau_b = 1$ (b) $f_r\tau_b = 2$ (c) $f_r\tau_b = 3$

Figure 5.7: For Gaussian distribution of 20 slices 1 ring, showing real (blue) and imaginary (red) coherent tunes in the presence of increasing wake field strength.

sponding plot for the airbag in Fig. 5.2, but the right hand side of the graph has a much stronger maximum imaginary coherent tune. Initially, we can see that like for the airbag distribution, increasing space charge lifts the TMCI due to wake fields.

We can start by examining the effect of increasing wake field strength on the coherent tunes for $f_r\tau_b$ equal to 1, 2 and 3, shown in Fig. 5.7. Comparing to theory, we see different real (blue) modes coupling for all three $f_r\tau_b$, where for $f_r\tau_b = 3$, the mode coupling is a lot clearer than for the airbag model, where we now see the first coupling to be that of -2 and -3 (marginally occurring for a lower normalised intensity than modes 0 and -1). We also see that the TMCI threshold has increased compared to for the airbag, increasing more for increased $f_r\tau_b$, hence the most significant difference is for $f_r\tau_b = 3$ where the TMCI threshold is at a normalised intensity of 23.5 compared to 16.2 for the airbag.

Like for the airbag, we need to investigate the cause of the imaginary coherent tune for higher space charge, as shown in Fig. 5.6 in the region above space charge strength of 3.5. Hence, just as we decreased the ring width of the airbag model to see if part of our result was

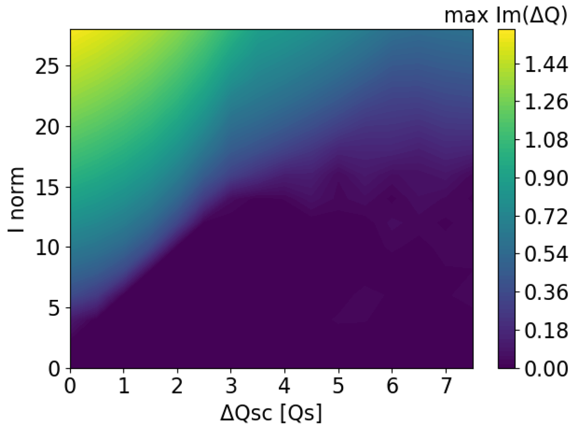

(a) $f_r \tau_b = 1$

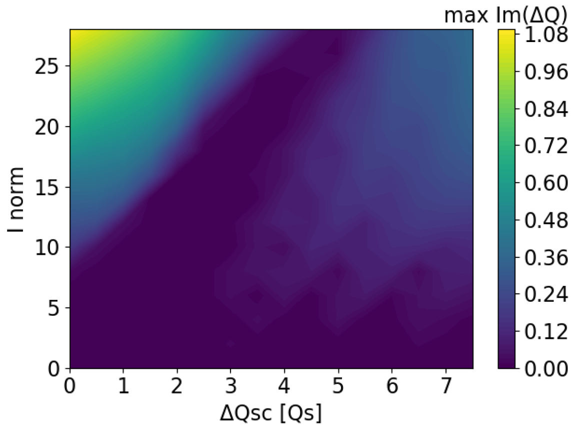

(b) $f_r \tau_b = 2$

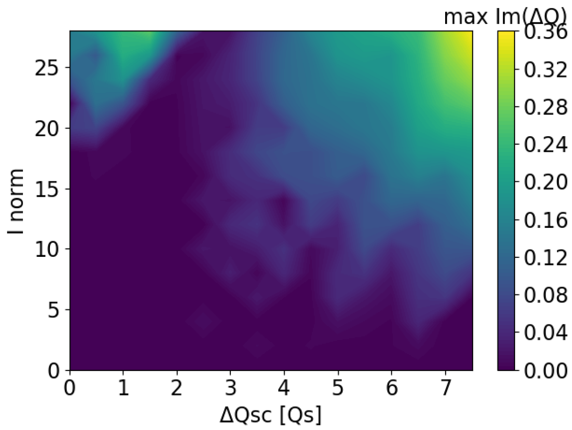

(c) $f_r \tau_b = 3$

Figure 5.8: Contour plots of the maximum imaginary tune shift for theoretical space charge tune shift against normalised wake field intensity for a Gaussian distribution of 20 slices 10 rings.

due to our numerical computation, the equivalent for the Gaussian distribution is increasing the number of rings and slices. Furthermore, we increased the number of rings so that we have a beam discretisation of cells divided by 20 slices and 10 rings. This produced the contour plots in Fig. 5.8, showing how the strength of the imaginary coherent tune for $f_r \tau_b$ equal to 1, 2 and 3 varies with space charge and wake field strength. There is still the distinct top left corner of instability but the right hand side of all three plots have drastically reduced in imaginary coherent tune strength, and also all exhibit different behaviour. The contour plots give us our primary indicator that for increased radial modes, all areas of instability vary with $f_r \tau_b$, a function of the wake field, and thus should be considered when looking at the TMCI.

In Fig. 5.8a for $f_r \tau_b = 1$, we see that space charge no longer completely suppresses the TMCI due to the wake field like in Fig. 5.6. We can take a closer look at this behaviour by looking at the comparison between the discretisation of the beam for 20 slices with 1 ring and 10 rings for a fixed wake of $I_{norm} = 25$ for varying space charge parameter, as seen in figures 5.9a and 5.9b, respectively. The radial modes produced by having 10 rings make it difficult to see where the instabilities occur on the real plot, so we decided to colour code the imaginary tune shifts by their strength, where red is the highest, decreasing in shade to orange and then to yellow which represents zero and below. This highlights where on the real plot the instability occurs in order to distinguish which mode is responsible for the coupling. In Fig. 5.9a which only considers radial mode 0, there are two distinct sections of imaginary tune presence. We can see azimuthal modes 0 and -1 decouple at a space charge strength of 3.9 and consequent coupling of positive mode pairs 0,2 and 1,3. Now comparing to Fig. 5.9b where we have 10 radial modes per azimuthal mode, we see the plot showing the imaginary coherent tune is very different. We can see that there are three distinct lines of instability highlighted on the real plot, where the strongest instability (red) is caused by the wake field for azimuthal mode -2, which decouples at a space charge strength of approximately 5.4. This instability is similar in placement to the coupling due to wake fields in Fig. 5.9a and likely corresponds to the same TMCI. We also see the next strongest line in orange stems from azimuthal mode 0, implying the increase in radial modes has uncovered another TMCI due to wake fields. However, it doesn't decouple within the strength of the space charge tested. This is a new result that we did not see appearing with the airbag model, where the space charge was always successful at suppressing the instabilities caused by the wake fields. This coupling implies that the space charge doesn't suppress the TMCI due to wake fields at the same definitive rate as for the airbag. We also have the third line of instability which is caused by the coupling of modes 1 and 2 for a space charge strength of 1, hence it is a result of increased space charge, rather than the wake field. This instability is also significant in that it grows in strength for increasing space charge. This implies that increasing space charge lifts the TMCI due to wake fields, but also produces TMCI between other modes. To check this is a valid TMCI due to increased space charge and not due to our computation, we should compare to a thinner beam discretisation.

Increasing the beam discretisation to 40 slices and 20 rings, we get the corresponding plot in Fig. 5.9c. We see that the imaginary coherent tunes are very similar to Fig. 5.9b, with the same three distinct lines of instability on the real plot for modes -2, 0 and notably the resulting coupling of modes 1 and 2. The presence of this positive mode coupling strengthens our claim that it is a valid TMCI caused by space charge. In addition, we can see at high space charge there is an increased number of instances of mode coupling and decoupling represented by small bubbles of imaginary tunes appearing. This implies that increasing the number of rings and slices could reveal more TMCI due to space charge until the distribution is converged to show the full effect of high space charge. For the instability induced by the wake field for azimuthal mode zero, we can now confirm that space charge suppresses the instability at a space charge strength of 7.2. This agrees with the airbag that space charge suppresses the TMCI due to wake fields.

Now, going back to the contour plots for a Gaussian distribution of 20 slices and 10 rings in figures 5.8b and 5.8c for $f_r\tau_b$ equal to 2 and 3, we see that they exhibit mesh-like patterns of instability for increased space charge. There are also no wake field only induced

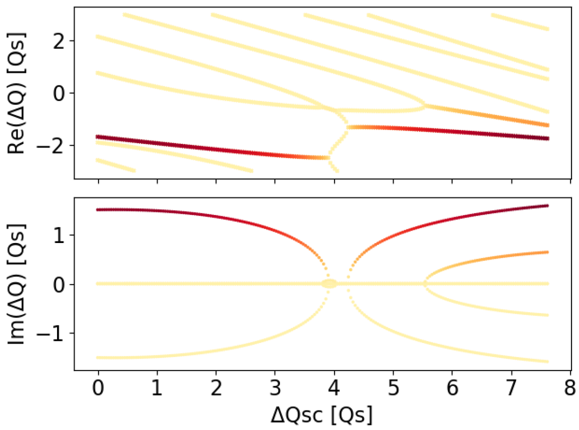

(a) 20 slices 1 ring

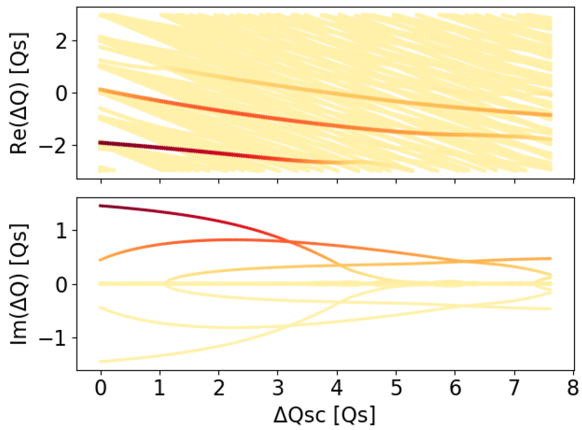

(b) 20 slices 10 rings

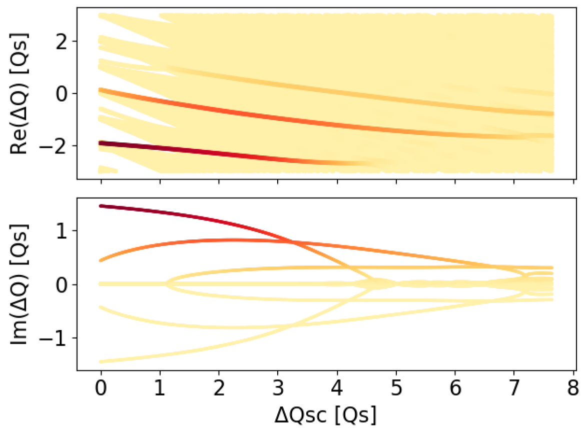

(c) 40 slices 20 rings

Figure 5.9: For Gaussian distribution plots of coherent tunes for varying space charge strength with constant wake of $I_{norm} = 25$ for $f_r \tau_b = 1$. Colour coding reflects strength of imaginary tune shift from yellow at zero or below to dark red for the strongest.

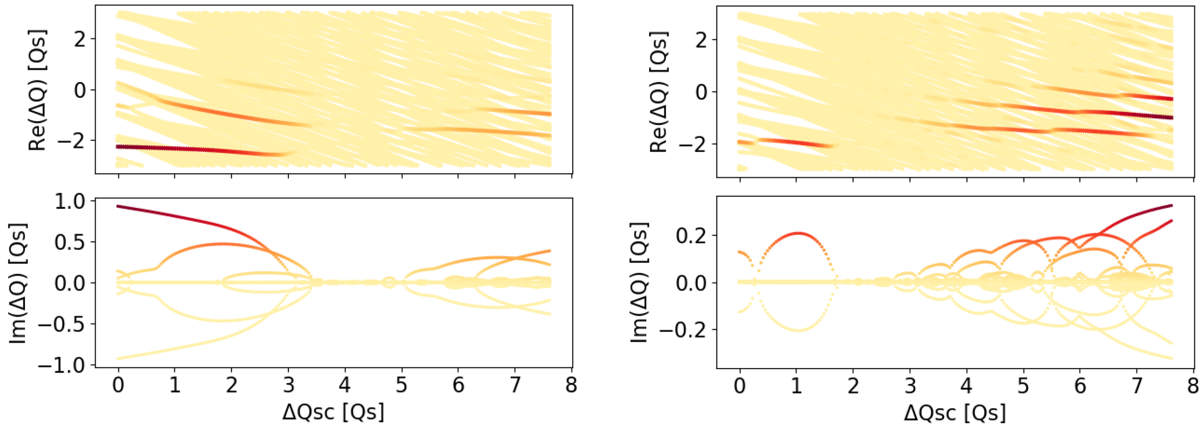

(a) $f_r\tau_b = 2$

(b) $f_r\tau_b = 3$

Figure 5.10: For Gaussian distribution of 20 slices and 10 rings, plots of theoretical space charge tune shift against resulting real and imaginary simulated tune shifts for a fixed wake of $I_{norm} = 25$.

instabilities which survive through increased space charge, at this range. To examine the behaviour of the mesh-like imaginary tune observed, we again set the wake to be fixed at a normalised intensity of 25 and varied the space charge strength for both $f_r\tau_b$ equal to 2 and 3 to get the resulting real and imaginary coherent tune modes, shown in Fig. 5.10. Firstly, we can see that increasing $f_r\tau_b$ of the wake field decreases the strength of the imaginary tune, if we compare the ranges of the imaginary tune axes. Starting with $f_r\tau_b = 2$, we have the strongest instability stemming from azimuthal mode -2, where it is completely suppressed by space charge at a space charge strength of 3.1. We see the familiar shape of the imaginary tune mode evolution where the space charge suppresses the TMCI due to wake fields almost completely before instabilities occur again. For $f_r\tau_b = 3$ in Fig. 5.10b, the instabilities arising for a space charge parameter above 2.5 have an intriguing bubble-like pattern on the imaginary tune plot, signifying two real modes coupling and decoupling. Hence, we see a lot of positive mode coupling and decoupling, with increasing imaginary tune magnitude as the space charge strength increases.

Again, to confirm the instabilities generated at high space charge are valid, we increased the beam discretisation to 40 slices and 20 rings. In Fig. 5.11 we see the corresponding graphs of coherent tune for a fixed wake of normalised intensity 25 and varying space charge. Starting with Fig. 5.11a compared to Fig. 5.10a, they again show similar patterns in imaginary tune, implying the TMCI due to high space charge is valid. The increased beam discretisation seems to more clearly show that the space charge suppresses the instabilities due to wake fields as there are no longer any small instabilities occurring in the middle section of the graphs before space charge induces more instabilities. For high space charge, the instabilities have a lower imaginary tune, which is also seen in Fig. 5.11b. There are also more bubbles of coupling and decoupling exhibited, as well as more short lines of instability shown in the real plot, as the increased number of beam cells has been able to capture more accurately all the TMCI due to high space charge. It is clear that the instabilities are growing

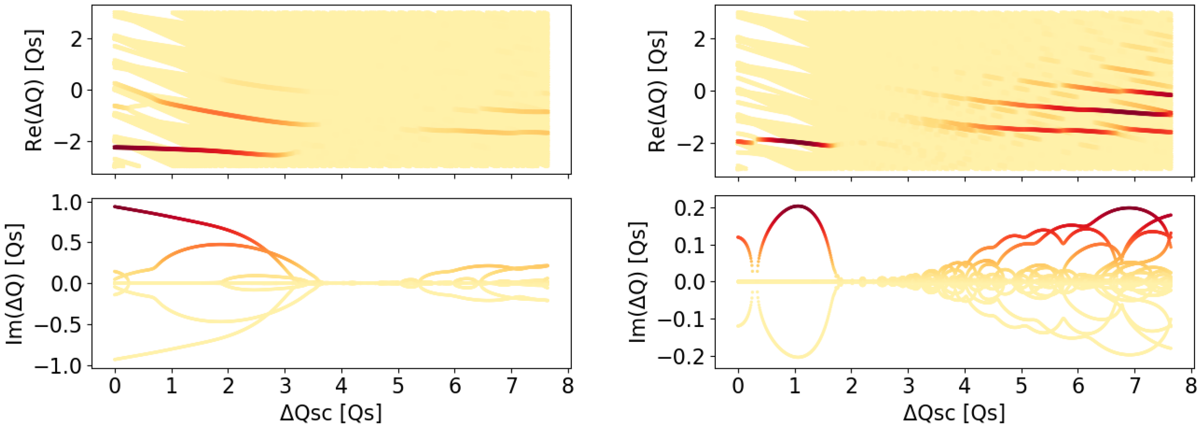

(a) $f_r\tau_b = 2$ (b) $f_r\tau_b = 3$

Figure 5.11: For a Gaussian distribution of 40 slices and 20 rings, the real and imaginary tune shifts are shown as a result of varying space charge and fixed wake field of $I_{norm} = 25$.

with increased space charge from looking at the growing cone-like shape of the bubbles. This implies that if we kept increasing the space charge parameter, the TMCI due to space charge could grow to be higher in imaginary tune strength than those induced by the wake field. This validates how space charge can be a limiting factor for hadron synchrotron operation.

5.3 TMCI comparison of airbag and Gaussian

We saw that for both the airbag and Gaussian distributions, increasing $f_r\tau_b$ increased the TMCI threshold and increasing space charge lifted the TMCI generated by wake fields. For the airbag model, for increased space charge, positive mode coupling was attributed to numerical artefacts, as a result of our approximation to a finite width. Our new result was that for the Gaussian distribution, we also witnessed positive mode coupling when space charge was increased, however with increased beam cell discretisation due to more rings and slices, we were able to verify that they were valid TMCI. We can thus see the difference between the two distributions, since the Gaussian distribution considers the positive mode coupling that is caused by space charge. This instability produced by increased space charge likely corresponds to the instability observed in some machines and is the difference we aimed to model.

However, we were not able to compare the results for the Gaussian distribution with a converged beam discretisation. This is such as increasing to 60 slices, 30 rings and 80 slices, 40 rings to see at which configuration increasing the number of rings and slices did not add more positive TMCI to the graphs. This would allow us to determine the full extent of how space charge affects the limitation due to electromagnetic wake fields.

Chapter 6

Conclusion

This project aimed to extend the code BimBim to include the effect of space charge and analyse the TMCI generated by the combination of space charge and wake fields for the airbag and Gaussian distributions. We were successful in implementing space charge and were consequently able to compare the space charge tune shifts and TMCI for the two distributions to showcase their differences. Both distributions exhibited space charge tune shifts similar in evolution to the analytical airbag in a square-well, where the most significant difference was that the Gaussian distribution was able to consider both azimuthal and radial modes, and had positive modes that crossed mode zero for increased space charge. For the TMCI analysis, both distributions initially exhibited space charge suppressing the TMCI due to wake fields. We found the Gaussian distribution seemed to be more compatible with reality by the presence of TMCI for increased space charge, similar to experimental data found in [3], whereas for the airbag these instabilities were attributed to numerical artefacts of our computation. The production of TMCI between positive modes due to space charge in the presence of wake fields is the new prediction found in this work, relevant for space-charge dominated machines.

There are several aspects of this work that can be improved. Notably, our method of convergence was numerically demanding for the Gaussian distribution with a more fine beam discretisation, resulting in us not being able to find the converged number of rings and slices. Hence, a less time-consuming method could be to only look at the convergence of the space charge interaction matrix elements which interact, rather than the matrix as a whole. The matrix contains many zeros that are calculated when looking at the whole matrix, hence this method could save a lot of time as it only focuses on non-zero elements. As mentioned, the analytical spectrum of the airbag with an infinitely thin ring width in a linear potential could have been plotted to confirm that the positive mode couplings due to increased space charge were due to our approximation to a finite ring width. We approximated the ring to be finite because for an infinitely thin ring, there were diverging matrix terms and thus it was very numerically demanding to reduce the width further. However, it has been found that the diverging terms can be mitigated by changing the set-up slightly by tilting all the slices by a small angle [17]. We could also have extended the work such that we simulated the space charge tune shifts for an airbag square-well distribution so that we could compare more accurately to the analytical spectrum, which we used as our relation to theory in Sec. 4.1.

Since this approach is novel in the field of beam instabilities with space charge forces, there is a lot of exciting future work that can be done to extend this project. Moving forward after modelling instabilities could thus be to generate experimental data to back up our findings, conduct more research on their behaviour with other collective effects or finding ways to mitigate them. An outlook for this work could be to show that our predictions are true by quantitative comparison with experimental data, which could be done, for example, with the Super Proton Synchrotron at CERN. Tune shift modes are difficult to see in machines hence instead, we could compare with data from a known machine observable such as looking at the effect on the intra-bunch motion for each turn. A simple attempt at mitigation could be to see the effects of adding a transverse feedback, which acts as a damper in order to increase the stability of the beams [19]. Another possible technique of mitigation we can consider is that of chromaticity [20]. We could thus seek to quantify how effective such a mitigation could be as well as observe which regions of instability it can be successful on. Lastly, this work could be extended to also look at the non-linear force of space charge, as it has been found that Landau damping suppresses TMCI that chromaticity and transverse feedback are not successful at damping [15].

Acknowledgements

I'd like to thank Imperial for allowing me to study abroad and EPFL for accepting my application, especially Gavin Davies for his support throughout the year. I'd like to thank the LPAP group at EPFL for being so welcoming and Tatiana Pieloni for being so supportive and notably setting up this project for me, as well as teaching me about accelerator physics in her class "Introduction to particle accelerators." Most importantly, I'd like to thank my supervisor Xavier Buffat who has been exceptional in guiding me through this research experience. I am also very grateful to have been able to experience a true research environment by undertaking some of my project on-site at CERN. Lastly, I'd like to thank my loving parents for their amazing support in everything that I do.

Bibliography

[1] A. Wolski, *Beam Dynamics in High Energy Particle Accelerators*. World Scientific, 2014.

[2] A. Chao, *Physics of Collective Beam Instabilities in High Energy Accelerators*. John Wiley and Sons Inc., New York, 1993.

[3] H. Bartosik, "Beam dynamics and optics studies for the LHC injectors upgrade," Ph.D. Thesis, TU Vienna, Austria, 2013. [Online]. Available: http://cds.cern.ch/record/1644761

[4] M. Blaskiewicz, "Fast head-tail instability with space charge," *Phys. Rev. ST Accel. Beams*, vol. 1, *(4)*, pp. 044201, 1998. Available: https://link.aps.org/doi/10.1103/PhysRevSTAB.1.044201. DOI: 10.1103/PhysRevSTAB.1.044201.

[5] A. Burov, "Head-tail modes for strong space charge," *Phys. Rev. ST Accel. Beams*, vol. 12, *(4)*, pp. 044202, 2009. Available: https://link.aps.org/doi/10.1103/PhysRevSTAB.12.044202. DOI: 10.1103/PhysRevSTAB.12.044202

[6] L. Rivkin and T. Pieloni. (2019). Introduction to Particle Accelerators. EPFL, Switzerland. [Lecture Handout]. Available: https://moodle.epfl.ch/pluginfile.php/2304475/mod_resource/content/1/booklet.pdf

[7] E. Gottlob, "Implementation of Space Charge Forces in BimBim," Thesis, EPFL, Lausanne, Switzerland, 2018. [Online]. Available: https://cds.cern.ch/record/2298900

[8] T. Pieloni. (2019). Luminosity and Beam-Beam Effects in the Large Hadron Collider. EPFL, Switzerland. [PowerPoint slides]. Available: https://moodle.epfl.ch/mod/resource/view.php?id=1046750

[9] J. Gareyte. (July 2000). Transverse Mode Coupling Instabilities. Presented at Conf. on High Quality Beams, Moscow, Russia. [Online]. Available: https://cds.cern.ch/record/477074/files/sl-2000-075.pdf

[10] N. Asmar, *Partial Differential Equations with Fourier Series and Boundary Value Problems*, 2nd ed. Pearson Prentice Hall, 2005.

[11] K. Schindl. (Sep. 2003). Space Charge. Presented at CERN Accelerator School pp.305-320, Zeuthen, Germany. [Online]. Available: https://cds.cern.ch/record/941316/files/p305.pdf

[12] M. Ferrario, M. Migliorati, and L. Palumbo. (Oct. 2015). Space Charge Effects. Presented at CERN Accelerator School, Warsaw, Poland. [Online]. Available: https://indico.cern.ch/event/361988/contributions/1775745/attachments/1157672/1678600/Space_Charge_Final.pdf

[13] H. Wiedemann, "Wake Fields and Instabilities*", in *Particle Accelerator Physics*, Ed., Springer Int. Pub., 2015, ch. 22, pp 737-796. [Online]. Available: https://doi.org/10.1007/978-3-319-18317-6_22.

[14] X. Buffat, "Transverse Beams Stability Studies at the Large Hadron Collider," Ph.D. Thesis, EPFL, Lausanne, Switzerland, 2015.

[15] S. Antipov et al., "MD 4145: Study of Landau damping with an Antidamper," CERN, Meyrin, Switzerland, Rep. CERN-ACC-NOTE-2019-0034, Aug. 2019. Accessed: 29 June 2020. [Online]. Available: http://cds.cern.ch/record/2685297

[16] A. Oeftiger, "Space Charge Effects and Advanced Modelling for CERN Low Energy Machines," Ph.D. Thesis, EPFL, Lausanne, 2016.

[17] X. Buffat, "Beam stability without eigenvalues: The impact of space-charge on the TMCI," in *HSC section meeting*, CERN, Switzerland, 22 June 2020.

[18] E. Metral, X. Buffat and G. Rumolo, "Transverse mode-coupling instability in the presence of detuning impedance," CERN, Meyrin, Switzerland, Rep. CERN-ACC-NOTE-2020-0019, 7 Apr. 2020. Accessed: 15 June 2020. [Online]. Available: http://cds.cern.ch/record/2714848/files/CERN-ACC-NOTE-2020-0019.pdf

[19] E. Metral, "Effects of transverse damper, detuning impedance, linear coupling, chromaticity, Landau damping and space charge on TMCI," in *Space charge workshop*, CERN, Switzerland, 5 Nov. 2019. [Online]. Available: https://indico.cern.ch/event/828559/contributions/3528530/attachments/1939176/3214686/SCandCoherentInstabilities_EM_05-11-2019.pdf

[20] T. Nakamura et al., "Chromaticity for energy spread measurement and for cure of transverse multi-bunch instability in the SPring-8 storage," *PACS2001. Proceedings of the 2001 Particle Accelerator Conference (Cat. No.01CH37268)*, Chicago, IL, USA, 2001, pp.1972-1974 vol.3, doi:10.1109/PAC.2001.987246